Journal of Materials Chemistry C

ROYAL SOCIETY OF CHEMISTRY

PAPER

View Article Online
View Journal

Cite this: DOI: 10.1039/d5tc03478g

Adaptive self-powered photodetection and neuromorphic computing in a $CuCrP_2S_6$ ionotronic device

Yanan Cao,†[a] Wan Wang,†[ab] Jiao Peng,†[c] Xin Chen,[ab] Yezhao Zhuang,[b] Bo Peng,[d] Lu Cheng,[e] Zhipeng Zhong,[b] Jianlin Shi,[b] Xiang Li,[b] Wu Shi,[f] Jianlu Wang,[b] Junhao Chu[b] and Hai Huang *[b]

In-sensor computing devices integrating sensing and processing functions are emerging as key enablers for next-generation artificial vision systems. Their development critically depends on identifying materials capable of mimicking the adaptive, multimodal behavior of biological synapses. Here, we demonstrate $CuCrP_2S_6$ (CCPS), a two-dimensional metal thiophosphate, as an optoelectronic neuromorphic material that simultaneously supports photodetection and synaptic plasticity. A CCPS photodetector exhibits both strong photoconductive behavior and a self-powered photoresponse at zero bias through directional ion migration. The vertical device architecture exhibits an intrinsic photoresponsivity of 420 mA W^{-1} and a specific detectivity of up to 3.5×10^{10} Jones. Crucially, both the magnitude and polarity of the photovoltaic current can be reversibly tuned by controlling ionic migration, mimicking the long-term potentiation and depression. A CCPS-based photonic synapse network achieves 89.8% image recognition accuracy on the Fashion-MNIST dataset, approaching the full-precision benchmark. Furthermore, a 3×3 CCPS photodetector array enables a programmable spatial light response, facilitating in-sensor image preprocessing such as edge enhancement. This work highlights CCPS as a multifunctional material platform for integrated perception–computation electronics and paves the way for intelligent, on-chip visual processing systems.

Received 18th September 2025,
Accepted 15th March 2026

DOI: 10.1039/d5tc03478g

rsc.li/materials-c

Introduction

In-sensor computing electronic devices, which integrate visual perception and edge processing, hold tremendous potential for application in next-generation artificial vision systems.[1–3] By enabling direct signal processing at the sensor level, these systems can significantly reduce redundant data storage, lower transmission energy consumption, and improve the overall computational efficiency.[4] Such architecture departs from the conventional ''sense–transmit–compute'' paradigm, offering a promising route toward overcoming energy bottlenecks in modern information electronics.

A key to advancing in-sensor computing devices lies in identifying functional materials tailored for biomimetic visual tasks.[5] In this context, ionic conducting materials have attracted growing attention due to their unique ion–electron coupling mechanisms. Their inherent advantages—including synaptic plasticity, photosensitivity, and multimodal sensing capabilities—render them highly promising for neuromorphic visual systems.[6] Among various candidates, metal thiophosphate (MTP) materials have attracted considerable interest due to their ionic migration behavior.[7–9] The conductivity of the MTP device can be modulated through reversible ion migration, enabling synaptic-like plasticity, which is highly desirable for neuromorphic computing devices.[10,11] Numerous studies[12] have focused on tuning ion transport mechanisms and optimizing device architectures based on these materials. In our previous work, we systematically investigated $CuCrP_2S_6$ (CCPS), a representative member of the MTP family, and demonstrated that its conductivity can be precisely modulated by electrical pulses, allowing for stable and highly controllable multilevel conductance states.[13] This characteristic has enabled

[a] State Key Laboratory of Digital Intelligent Technology for Unmanned Coal Mining, Anhui University of Science and Technology, Huainan, 232001, China
[b] State Key Laboratory of Photovoltaic Science and Technology, Shanghai Frontiers Science Research Base of Intelligent Optoelectronic and Perception, Institute of Optoelectronics and College of Future Information, Fudan University, Shanghai, 200433, China. E-mail: huangh@fudan.edu.cn
[c] West Anhui University, Lu'an, Anhui, 237012, China
[d] College of Smart Materials and Future Energy, Fudan University, Shanghai, 200433, China
[e] Institute of Biomedicine, University of Eastern Finland, Kuopio, 70210, Finland
[f] State Key Laboratory of Surface Physics and Institute for Nanoelectronic Devices and Quantum Computing, Fudan University, Shanghai, 200433, China
† These authors contributed equally.

high image and audio recognition accuracy in convolutional neural network (CNN)[14]-based recognition tasks, highlighting its promise for high-precision neuromorphic computing applications. However, existing research has primarily focused on the electrical synaptic behavior of CCPS,[15] while its optoelectronic synaptic properties remain largely unexplored, limiting its potential for integrated perception–computation systems. Given that CCPS is also a layered two-dimensional semiconductor, it also holds substantial potential for photoresponsive neuromorphic devices. Therefore, a comprehensive investigation into its optoelectronic synaptic behavior is essential for unlocking its full potential in intelligent vision systems.

In this work, we systematically investigated the optoelectronic properties of CCPS photodetectors and explored their potential in optoelectronic neuromorphic applications. We demonstrate that the CCPS photodetector exhibits not only a strong photoconductive response but also a self-powered photoresponse at zero bias, enabled by the directional ion migration. The vertically structured CCPS device achieves a high photoresponsivity of 420 mA W^{-1} and a specific detectivity of up to 3.5×10^{10} Jones, underscoring its potential in low-light imaging and self-powered sensing applications. Moreover, by modulating the direction and extent of ionic transport, both the magnitude and polarity of the photocurrent can be reversibly tuned. This enables the emulation of long-term potentiation (LTP) and long-term depression (LTD)-like synaptic behaviors under controlled electrical stimuli. Leveraging this optoelectronic plasticity, we construct a CCPS-based neuromorphic photonic synapse network,[16,17] achieving a recognition accuracy of 89.8% on the Fashion-MNIST image dataset, approaching the full-precision simulation benchmark of 92.7%. Furthermore, a 3 × 3 CCPS photodetector array is fabricated, wherein the polarity-tunable photocurrent of each unit enables the programmable spatial response matrices. This functionality allows for in-sensor image preprocessing, including edge enhancement and contrast sharpening, offering a promising route toward on-chip intelligent perception–computation systems.

Results

The CCPS photoconducting device was fabricated through mechanical exfoliation combined with a dry transfer technique, followed by electron beam lithography and a standard lift-off process (see the Methods section). Previous studies have demonstrated that CCPS exhibits an ultralow dark current, and its photoresponse can be effectively enhanced by reducing the channel length while maintaining the low dark current level.[18] Therefore, the photoresponse characteristics of CCPS were firstly investigated using an ultra-short channel photodetector, in which CCPS nanoflakes are sandwiched between few-layered graphene (FLG) electrodes, as illustrated in Fig. 1a. The optical microscopy image of the photodetector device is shown in Fig. 1b, showing the uniform thickness and high-quality interfacial integrity of both the CCPS and graphene nanoflakes. The thickness of the layered materials is characterized by atomic force microscopy (AFM), with the thickness of

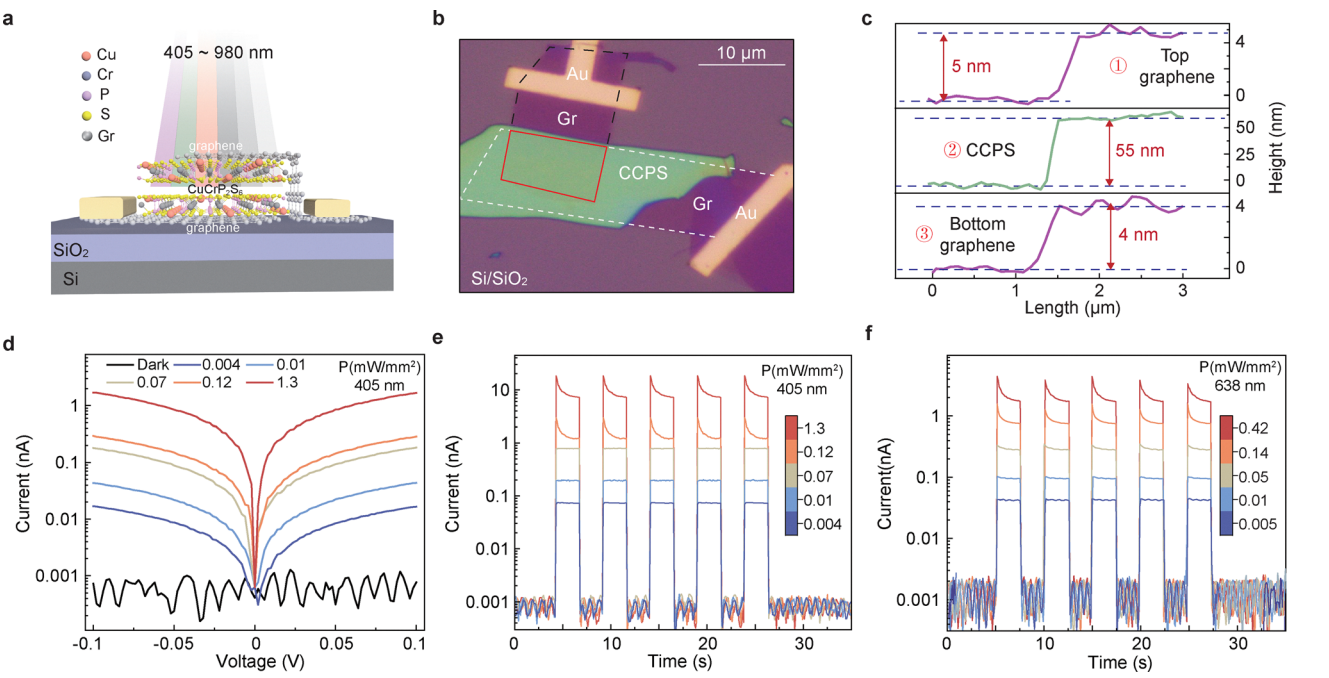

Fig. 1 Structure and photoresponse of the CCPS photodetector. (a) Schematic structure of the CCPS photodetector made with few-layered graphene (FLG) as the contact electrode. (b) Optical microscopy image of the CCPS photodetector made on the Si/SiO_2 substrate. (c) Thickness characterization of the CCPS and top and bottom FLG nanoflake through AFM, corresponding to the dashed lines in (b). (d) Output characteristics of the CCPS photodetector in the dark and under 405 nm illumination with varying intensities. Time-resolved photoresponse of the CCPS photodetector for 405 nm (e) and 638 nm (f) light at varying intensities under a 0.1 V bias.

the CCPS, bottom graphene, and top graphene layers measured to be approximately 55 nm, 4 nm, and 5 nm, respectively, as shown in Fig. 1c. The Raman spectrum of the CCPS shown in Fig. S1 (SI) verifies the high crystallinity of the CCPS layer, with characteristic peaks aligning with reported values.[19–21]

The photoresponse of the CCPS photodetector was systematically investigated at varying illumination wavelengths and intensities. Fig. 1d illustrates the current–voltage (I–V) characteristics of the CCPS photodetector both in the dark and under 405 nm illumination. The device exhibits a dark current as low as ~500 fA in the device with a CCPS thickness of 55 nm. A clear photoresponse can be observed at 405 nm with varying intensities. The time-resolved photoresponse to 405 nm is measured by periodically turning the light on and off, as shown in Fig. 1e, showing significant enhancement in photocurrent with increasing light intensity from 0.004 mW mm^{-2} to 1.3 mW mm^{-2}. The photo- to dark current ratio (I_{ph}/I_{dark}) reaches approximately 10^4 at 1.3 mW mm^{-2}. Similarly, the device shows a clear photoresponse to 638 nm light, as depicted in Fig. 1f.

Moreover, considering the moderate bandgap (1.0–1.2 eV) of the CCPS material as previously reported,[22,23] the device also shows a clear photoresponse to the near infrared (NIR) light from 785 to 980 nm. This observation is consistent with the absorption spectrum of CCPS obtained in our measurements, as shown in Fig. S2 (SI). At an incident optical power density of 3.4 mW mm^{-2} under 850 nm illumination, a maximum photocurrent ratio (I_{ph}/I_{dark}) of 10^2 is achieved, as shown in Fig. 2a. The photoresponses at other wavelengths (520 nm, 785 nm, and 980 nm) are shown in Fig. S3 (SI), demonstrating the broad-band spectral response of the CCPS-based photodetector. The relationship between photocurrent and light intensity is shown in Fig. 2b, demonstrating a sublinear relationship, $I_{ph} \propto P^{\alpha}$, where α is a constant with the value ranging from 0.76 to 0.84 when varying the light wavelength. This sublinear relationship is presumably attributed to the trap-assisted recombination process in the CCPS channel material.

The spectral response of the CCPS photodetector is measured at an identical light intensity of 0.4 mW mm^{-2}, as shown in Fig. 2c. The photocurrent increases as the wavelength reduces, which is consistent with the photon absorption spectrum of the CCPS material, as shown in Fig. S2 (SI). To estimate the specific detectivity of the photodetector, the spectral noise density is measured using a low noise analyzer, as shown in Fig. 2d. The measured noise at a 0.1 V bias is exceptionally low (around 10^{-14} A Hz$^{-1/2}$), outperforming many 2D material-based photodetectors, such as MoS_2 and WS_2.[24,25] This low noise level enables a high detectivity of 3.5×10^{10} Jones for 405 nm light with an intensity of 4×10^{-4} mW mm^{-2}, alongside a photoresponsivity of 420 mA W^{-1} (Fig. 2e), positioning the device as a competitive candidate for low-light detection.[26] The temporal response of the device under 405 nm illumination (Fig. 2f) exhibits a rise time of 37 ms and a fall time of 59 ms, making it sufficient for applications such as environmental sensing and industrial imaging. Overall, the CCPS

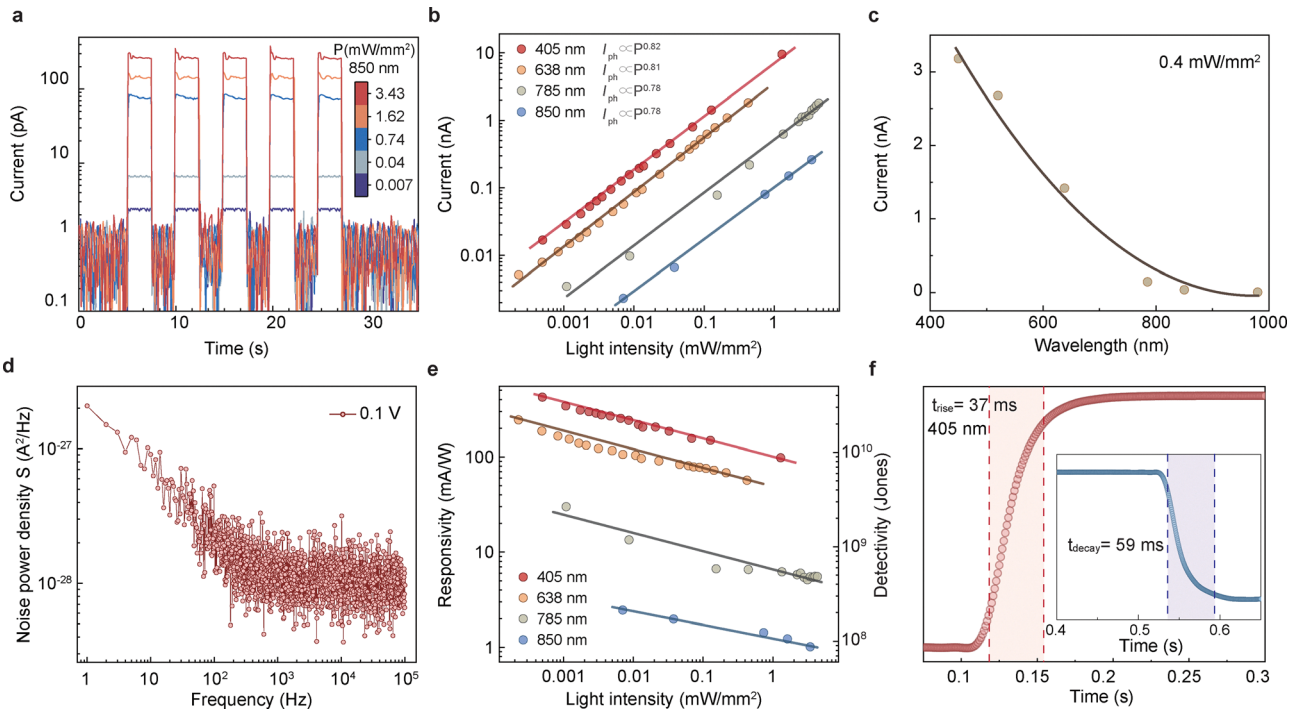

Fig. 2 Spectral response of the CCPS photodetector. (a) Time-resolved photoresponse of the CCPS photodetector for 850 nm NIR light under a 0.1 V bias. (b) Sublinear relationship between photocurrent and light intensity for varying wavelength of 405 nm, 638 nm, and 850 nm. (c) Spectral response of the CCPS photodetector from visible to NIR light at an identical light intensity of 0.4 mW mm^{-2}. (d) Spectral noise density measurement of the CCPS photodetector at a 0.1 V bias. (e) Photoresponsivity and specific detectivity for varying wavelengths (405 nm, 638 nm, 785 nm, and 850 nm) and intensities. (f) Rise and fall times of the CCPS photodetector under 405 nm light illumination.

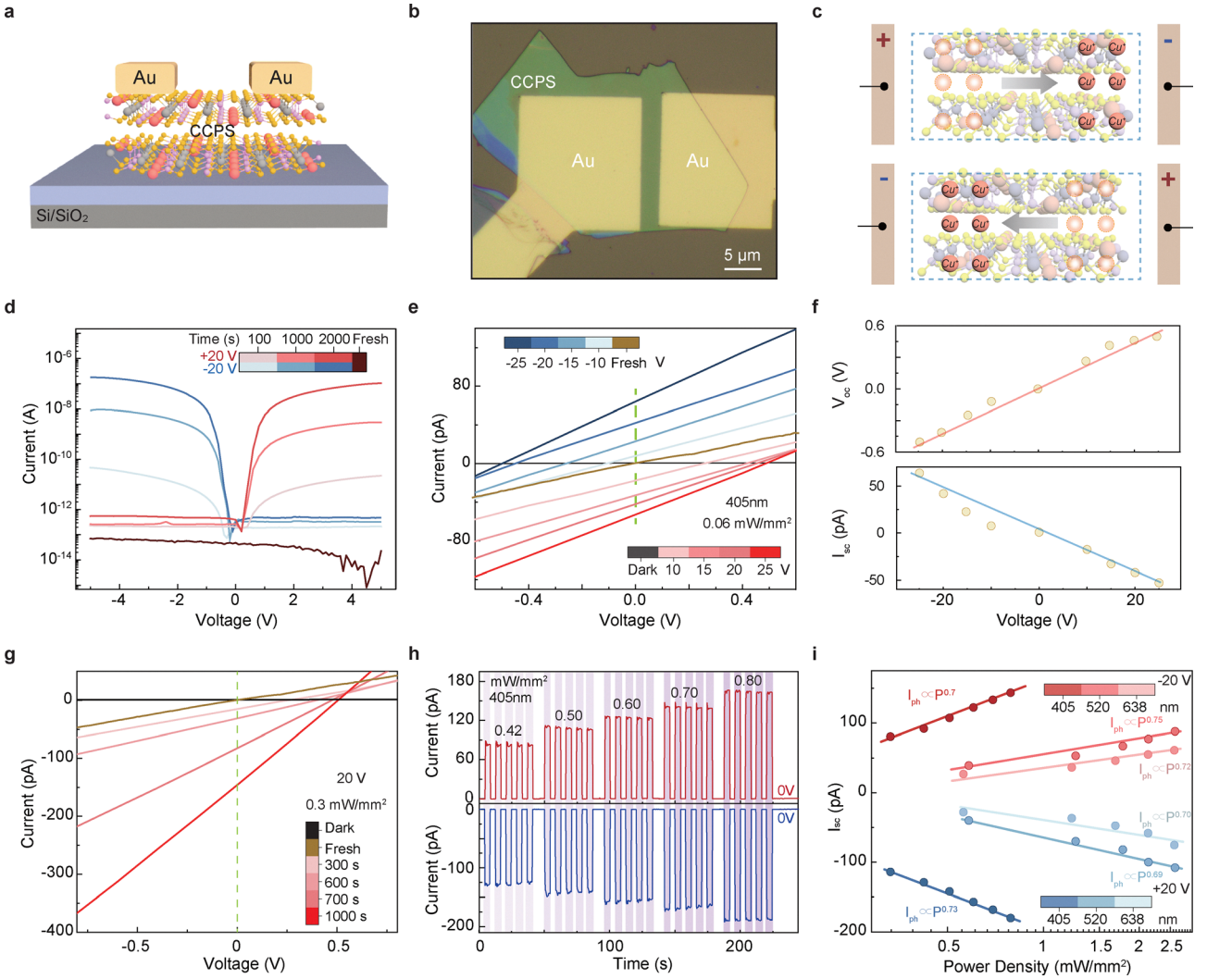

Fig. 3 Photovoltaic response of the CCPS photodetector. (a) Schematic structure of the CCPS photodetector in a metal–semiconductor–metal (MSM) scheme. (b) The optical microscopy image of the CCPS device; the scale bar represents 5 μm. (c) The schematic illustration of Cu migration under the bias electric field, and the direction switches with the applied voltages. (d) The rectification behavior of the CCPS device after ion migration, indicating the formation of homojunctions in the CCPS photodetector. The rectification ratio and direction change with the duration and direction of applied voltages (20 V). (e) *I*–*V* curves in the dark and under 405 nm illumination with an intensity of 0.06 mW mm^{-2} after ion migration driven by varying voltages from 10 to 25 V for 1500 s. (f) The V_{oc} and I_{sc} extracted from the *I*–*V* curves in (e), showing the dependence with the applied activation voltage. (g) *I*–*V* curves under 405 nm illumination (0.3 mW mm^{-2}) after activation by 20 V with varying durations from 0 to 1000 s, showing varying V_{oc} and I_{sc} values. (h) Time-resolved photoresponse under 405 nm illumination at zero bias after ±20 V activation for 650 s. (i) The relationship between I_{sc} and incident light intensity for 405 nm, 520 nm, and 638 nm light after activation by ±20 V for 650 s.

photodetector exhibits outstanding optoelectronic performance, including low noise, a high I_{ph}/I_{dark} ratio, excellent responsivity and detectivity, and fast rise and fall time. These features establish CCPS as a promising candidate for use in high-performance photodetector applications, with potential for further optimization across different wavelengths and intensities.

We further investigated the influence of the ionic conductance on the photoresponse behavior of CCPS photodetectors and explored their potential application in neuromorphic computing. A two-terminal CCPS photodetector with Cr/Au electrodes was fabricated on the Si substrate with 285 nm SiO_2. The schematic device structure and corresponding optical microscopy image are shown in Fig. 3a and b. The AFM image and the thickness (~50 nm) of the CCPS used in the photodetector are shown in Fig. S4 (SI). According to previous studies, the migration of Cu ions can be activated when the applied electric field exceeds a certain threshold,[26,27] and the migration direction can be reversibly switched by the polarity of the bias voltage, as illustrated in Fig. 3c. This directional ion migration modulates the contact barrier and induces a surface potential gradient, thereby giving rise to the rectifying behavior.[28,29] Fig. 3d displays the rectified *I*–*V* characteristics of the device after applying bias voltages of +20 V and −20 V. The rectification ratio is strongly dependent on the duration of the applied bias, reaching values as high as 10^5 after a ±20 V bias is applied for 2000 s. Moreover, the rectification direction can be reversed

by changing the polarity of the applied field. Importantly, the gradient in the surface potential indicates the formation of a built-in electric field induced by Cu ion migration, which facilitates efficient separation of photogenerated carriers under illumination, thereby giving rise to a photovoltaic response, as shown in Fig. 3e. After applying an activation voltage of +20 V for 1500 s, the device exhibits a significant photovoltaic effect under 405 nm illumination with an intensity of 0.06 mW mm^{-2}, achieving an open-circuit voltage (V_{oc}) of up to 0.5 V and a short-circuit current (I_{sc}) of approximately 52 pA. Furthermore, the polarity of the photovoltaic response can be reversed by applying a negative bias voltage, confirming the bidirectional tunability of the built-in electric field. Importantly, higher activation voltages enhance ion migration, resulting in a stronger photovoltaic response, as evidenced by the increase of I_{sc} and V_{oc} shown in Fig. 3f. Additionally, extending the duration of bias application further promotes Cu^+ ion redistribution, thereby amplifying the photovoltaic effect. Fig. 3g illustrates the photoresponse *I–V* curves under 405 nm illumination with activation times ranging from 300 to 1000 s under a 20 V bias, clearly demonstrating that prolonged activation leads to enhanced photovoltaic performance. The evolution of I_{sc} and V_{oc} as a function of the activation time under a 20 V bias is summarized in Fig. S5 (SI), showing the increase in I_{sc} and V_{oc} as the activation time increases from 0 to 1000 s. Further investigation was carried out on the detector's response to 520 nm and 638 nm laser illumination. At both wavelengths, the V_{oc} gradually increased with increasing bias voltage and bias application time, while the I_{sc} exhibited an enhancement in the opposite direction, as shown in Fig. S6 and S7 (SI).

The time-resolved photoresponse of the device under 405 nm illumination at varying intensities and zero bias is shown in Fig. 3h. The photocurrent exhibits a clear dependence on the illumination intensity, increasing progressively with higher light intensity, and notably, its direction can be reversibly modulated by controlling the direction of ionic migration. Photovoltaic responses under 520 nm and 638 nm illumination were also systematically studied by varying the activation voltage, activation duration, and light intensity (Fig. S8, SI), showing consistent behavior with the 405 nm response. Fig. 3i summarizes the photocurrent–intensity relationship for 405 nm, 520 nm, and 638 nm wavelengths under both forward and reverse ionic migration conditions. The dependence of responsivity and detectivity on optical power density at different wavelengths is presented in Fig. S9 (SI). The detector exhibits a rise time of 190 ms and a fall time of 200 ms under 405 nm illumination at zero bias, as shown in Fig. S10 (SI).

Our investigations demonstrate that the CCPS device exhibits a tunable photovoltaic effect, which can be dynamically modulated by external electrical bias. This unique capability positions CCPS-based self-powered photodetectors[30] as promising components for optoelectronic neuromorphic systems, particularly in imaging acquiring and recognition tasks.[31] To demonstrate this potential, we systematically evaluated bidirectional synaptic plasticity by applying ±3 V electrical pulses and monitoring the zero-bias photocurrent after each pulse. As shown in Fig. 4a and Fig. S11 (SI), both LTP[32] and LTD[33] of the photocurrent were achieved. Specifically, for devices with positive short-circuit current (I_{sc}), −3 V pulses (3 s duration) induced LTP, whereas +3 V pulses triggered LTD, with stable modulation over more than 30 cycles.[34] Further analysis shows that, in the positive photocurrent state, the extracted nonlinearity factors are N_{LTP} = 0.82 and N_{LTD} = 3.51. In contrast, in the negative photocurrent state, the corresponding nonlinearity factors are N_{LTP} = 0.38 and N_{LTD} = 1.96, as shown in Fig. S12 (SI). When I_{sc} was negative, reversing the pulse polarity resulted in mirrored behavior, highlighting the system's symmetric and reversible synaptic functionality. This bidirectional adaptability is essential for mimicking biological synapses.[35] Mechanistically, the migration of Cu^+ ions driven by the applied electric field dynamically reconfigures the built-in potential landscape, enabling precise and programmable modulation of the synaptic weight.[36]

This ionically driven synaptic mechanism enables adaptive feature extraction in a convolutional neural network (CNN) applied to the Fashion-MNIST classification task (Fig. 4b).[37] The Fashion-MNIST dataset comprises 60 000 training and 10 000 testing images.[38] Each image is a 28 × 28-pixel grayscale representation of 10 distinct clothing categories (*e.g.* T-shirts, trousers, coats, sandals and so on).[39] The CNN based on the forward and backward LTP/LTD behavior of the CCPS photodetector achieves recognition accuracies of 89.8% and 89.5% for Fashion-MNIST testing images, respectively, approaching the full-precision simulation result of 92.7% (Fig. 4c). ''Full-precision simulation'' refers to software-based inference using 32-bit floating-point weights under the same network architecture, representing the theoretical upper bound of performance in the absence of hardware-induced non-idealities, such as device nonlinearity, conductance fluctuations, and limited state resolution. The discrepancy between the experimental result (89.8%) and the full-precision simulation (92.7%) arises primarily from two factors. First, the inherent nonlinearity and asymmetry of the experimentally measured LTP/LTD conductance updates limit the precise mapping of ideal trained weights. Second, the finite number of accessible conductance states constrains the precision of weight representation. Confusion matrices (Fig. 4d and e) show high accuracy for visually distinct categories (*e.g.*, sneakers (class 7) and trousers (class 1)), while misclassification primarily occurs between visually similar items (*e.g.*, shirts (class 6) *vs.* coats (class 4) and pullovers (class 2) *vs.* dresses (class 3)) due to overlapping grayscale features. The bidirectional synaptic plasticity – enabled by Cu^+ ion migration under ±3 V pulses and sustained by 405 nm photovoltaic excitation – supports Hebbian-like learning.[40] Forward plasticity enhances feature selectivity by reinforcing dominant visual cues (*e.g.*, shoe soles), while reverse plasticity introduces slight variability and simultaneously maintains robust performance (accuracy drop of $< 0.3\%$).

In addition, we provide a qualitative summary of the long-term potentiation/long-term depression (LTP/LTD) nonlinearity and neuromorphic demonstration performance of the CCPS

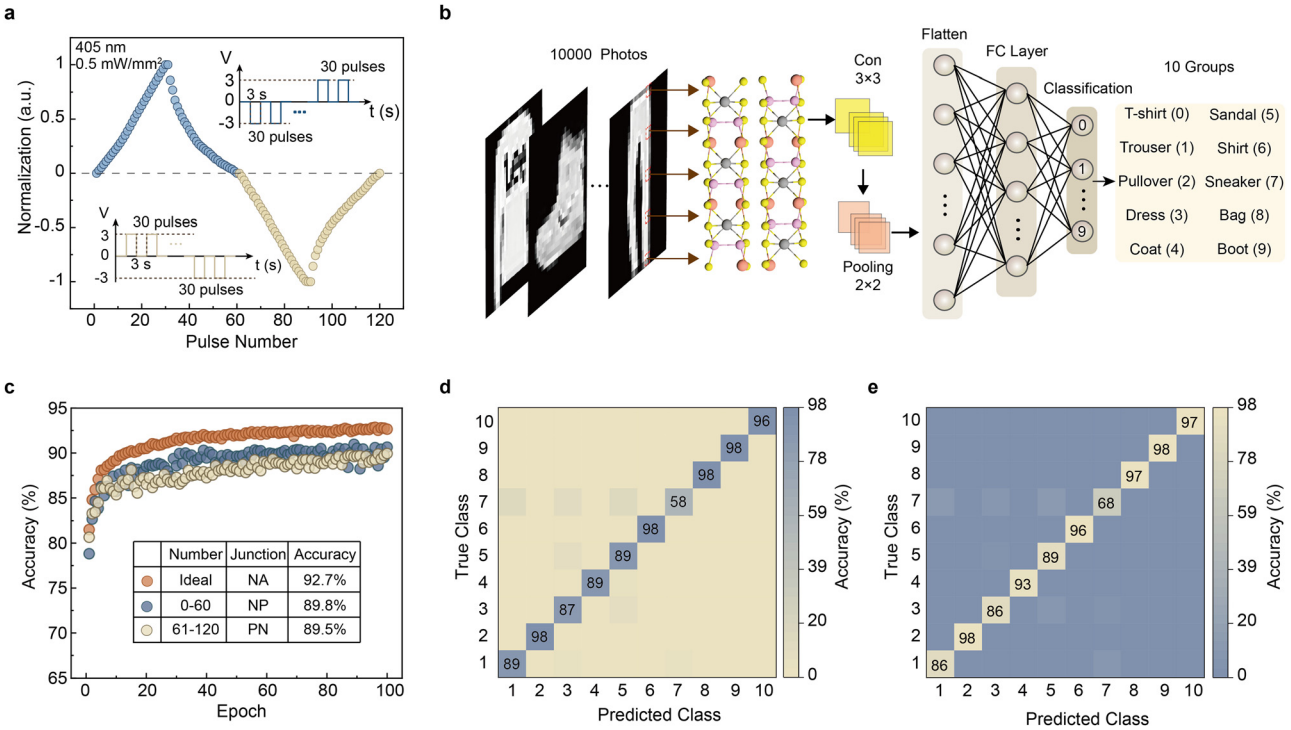

Fig. 4 Neuromorphic computation based on the tunable photovoltaic effect of the CCPS photodetector. (a) The I_{sc} of the CCPS device at 405 nm (0.5 mW mm^{-2}) exhibits LTP and LTD behavior by applying distinct voltage pulses. The LTP and LTD behaviors in the positive and negative direction were achieved by applying bias voltages of −3 V and 3 V with a duration of 3 s, respectively, as depicted in the inset. (b) Schematic of the convolutional neural network (CNN) architecture based on the CCPS device for the image classification using the Fashion-MNIST dataset. (c) Recognition accuracy for the Fashion-MNIST dataset using the experimentally measured LTP/LTD curves from both the positive and negative I_{sc} regimes, compared to the result from full-precision simulation. Confusion matrix for image classification using positive (d) and negative (e) LTP/LTD behavior, showing class-wise prediction accuracy across 10 clothing categories.

Table 1 Summary of synaptic characteristics and neuromorphic demonstration results of CCPS devices and representative reported materials

Material	Structure	Retention (s)	NL LTP/LTD	Network	Dataset	Demonstration accuracy (%)	Ref.
CCPS	Two terminals	2500	0.82/3.51	CNN	F-MNIST	89.8	This work
$CrSBr/WSe_2$	Three terminals	3000	0.17/0.32	ANN	F-MNIST	91.0	41
$Ag/Bi_2O_5Se/Au$	Two terminals	$\sim 10^3$	5.57/3.98	CNN	F-MNIST	85.0	42
$2H\text{-}MoTe_2$	Two terminals	$\sim 10^4$	0.006/0.015	DNN	F-MNIST	83.75	43
VP/MoS_2	Two terminals	—	1.3/2.2	FNN	F-MNIST	77.09	44
$ReSe_2$/h-BN/Gr	Three terminals	$\sim 10^3$	1.12/0.09	CNN	F-MNIST	88.99	45
Ag/MXene-ZrO_2 QDs/FTO	Two terminals	$\sim 10^3$	0.46/2.89	ANN	F-MNIST	84.2	46

device together with those of representative previously reported devices. This summary aims to place our results in the context of existing studies by highlighting device-level synaptic characteristics and their potential in neuromorphic computing tasks. The corresponding results are summarized in Table 1.

To further explore its function in image preprocessing and edge detection,[47] we fabricated a 3 × 3 CCPS photodetector array from a large-area exfoliated nanoflake, as shown in Fig. 5a. To verify the stability of the photovoltaic units in the array, the modulated devices were subjected to 1200 consecutive optical pulse cycles under 405 nm illumination at a 0 V bias, and no significant change in photocurrent was observed, demonstrating the stability of the array units, as shown in Fig. S13 (SI). Since the photoresponse of each pixel in the array can be modulated by controlling the degree of ion migration through applied bias voltage, the array enables the formation of various convolutional kernels for in-sensor computing.[48] We provided the programming conditions for the horizontal, vertical, and sharpening convolutional kernels. All programming voltages were applied for a fixed duration of 580 s, as summarized in Fig. S14 (SI). All experiments were conducted under 405 nm laser illumination with a power density of 0.14 mW mm^{-2}. The responsivity of each pixel was tuned by applying programmable bias voltages of varying magnitudes and durations, which determine the extent of ion migration and enable reconfigurable kernel patterns.[49] Compared to conventional three-terminal devices such as ferroelectric field-effect transistors,[50,51] the employed two-terminal bias-controlled modulation method offers a simpler and more practical operation scheme. Based on this approach, we programmed different

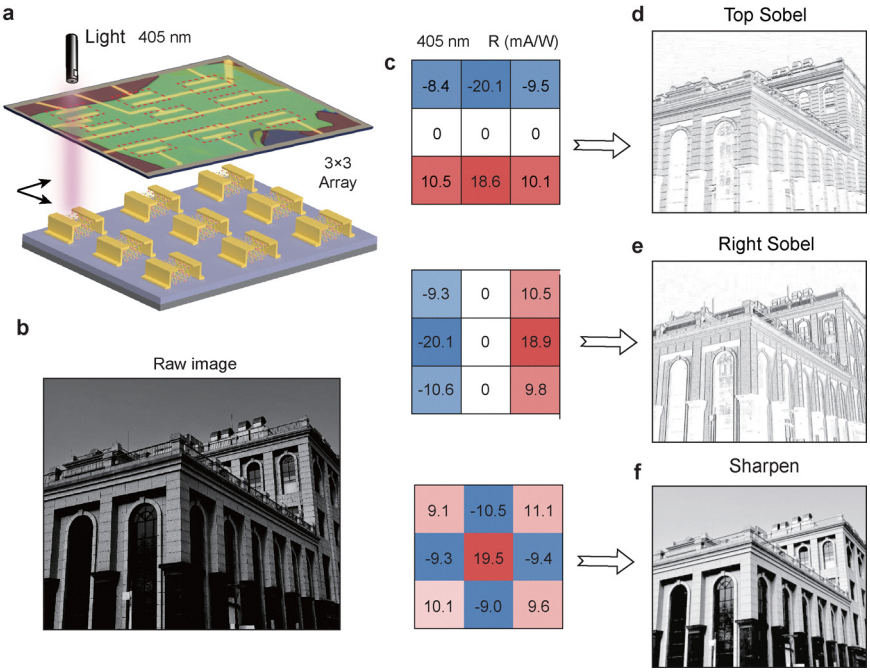

Fig. 5 Image preprocessing using the CCPS photodetector array. (a) Schematic structure of the 3 × 3 CCPS photodetector array. (b) Original grayscale image used for preprocessing demonstration. (c) Programmable construction of horizontal, vertical, and sharpening convolutional kernels *via* ion migration-controlled photoresponsivity under 405 nm illumination (0.14 mW mm^{-2}). Image preprocessing results using the three kernels, showing horizontal edge enhancement (d), vertical edge enhancement top (e), and contour sharpening (f), respectively.

response matrices across the 3 × 3 array to construct multiple convolutional kernels with the pixel-level photoresponsivity ranging from −20 mA W^{-1} to 20 mA W^{-1}. These convolutional kernels were then applied to a real-world grayscale image (Fig. 5b). As shown in Fig. 5c, by tailoring the spatial distribution of responsivity within each kernel, the system can perform various preprocessing functions, including horizontal edge enhancement[52] (Fig. 5d), vertical edge enhancement[53] (Fig. 5e), and contour sharpening[54] (Fig. 5f). These results highlight the potential of CCPS-based photodetector arrays for energy-efficient, hardware-level image processing directly at the sensor front-end.

Conclusions

In this work, we demonstrated a multifunctional CCPS-based photodetector system that integrates tunable photovoltaic behavior and ionically driven modulation mechanisms to enable in-sensor neuromorphic computing. By harnessing Cu^+ ion migration under external bias, the device exhibits dynamic and reversible photoresponse characteristics, enabling programmable synaptic plasticity such as LTP and LTD. This bidirectional synaptic functionality was leveraged to construct CNN for image recognition, achieving a high classification accuracy of 89.8% on the Fashion-MNIST dataset with minimal degradation compared to full-precision simulations. Furthermore, a 3 × 3 CCPS photodetector array was fabricated to realize reconfigurable convolutional kernels through spatially distributed responsivity profiles. This architecture facilitated diverse image preprocessing functions, including edge detection and contour sharpening, directly at the sensor level. The results highlight the potential of CCPS photodetectors as low-power, hardware-efficient building blocks for next-generation intelligent vision systems, offering a compact and scalable pathway toward integrated sensing–computation platforms.

Methods

Device fabrication and characterization

CCPS and few-layer graphene flakes were obtained *via* mechanical exfoliation of commercially sourced bulk crystals (Shenzhen Six Carbon Technology Co., Ltd) followed by deterministic transfer onto polydimethylsiloxane (PDMS) substrates. Flakes with a uniform optical contrast and smooth morphology were selected under an optical microscope (Olympus BX53M) for device assembly. The nanoflakes were then aligned and transferred to the silicon substrate with a 285 nm oxidation layer to form heterostructures. Then, methyl methacrylate (MMA) and polymethyl methacrylate (PMMA) were sequentially spin-coated onto the substrate at 4000 rpm for 60 s each. After spin-coating, the photoresist-coated silicon substrate was soft-baked on a hotplate at 180 °C for 3 minutes to remove residual solvents and improve adhesion. Cr/Au (10/50 nm) electrodes were deposited by thermal evaporation at a rate of 0.5 Å s^{-1}, following standard electron beam lithography (EBL) processes. Device geometry was optimized based on preliminary tests, with the channel length and width set to 3 μm and 40 μm, respectively, to minimize series resistance and enhance the

photocurrent response. The channel length and width of the array unit device were 4 μm and 15 μm, respectively.

Atomic force microscopy (AFM, Dimension ICON) was used to measure the thickness and confirm the flatness of exfoliated graphene and CCPS flakes. Raman spectroscopy (Renishaw inVia, 532 nm laser excitation) was conducted to verify the material composition, assess crystallinity, and detect interfacial interactions in the heterostructure. Electrical performance was measured using a Keithley 4200 SCS and a Keysight B1500A Semiconductor Device Parameter Analyzer using the lakeshore probe station under high vacuum conditions (10^{-6} Torr) to minimize environmental interference. Semiconducting diode lasers with varying wavelengths were used to measure the photoresponse of the device. The noise spectra were measured using a low-noise analyzer (Fs-pro, PRIMARIUS).

Author contributions

Yanan Cao: conceptualization, formal analysis, validation, visualization, writing – original draft, and funding acquisition. Wan Wang: data curation, formal analysis, validation, and visualization. Jiao Peng: formal analysis, validation, visualization, and writing – review and editing. Xin Chen: data curation, formal analysis, validation, and visualization. Yezhao Zhuang: simulation, validation, visualization, and writing – original draft. Bo Peng: formal analysis, methodology, and software. Lu Cheng: formal analysis, methodology, and software. Zhipeng Zhong: data curation and investigation. Jianlin Shi: data curation, investigation, and methodology. Xiang Li: data curation, investigation, methodology, visualization, and writing – original draft. Wu Shi: funding acquisition, and resources. Jianlu Wang: funding acquisition and resources. Junhao Chu: funding acquisition and resources. Hai Huang: conceptualization, data curation, funding acquisition, investigation, methodology, resources, supervision: lead, writing – original draft, and writing – review and editing.

Conflicts of interest

The authors declare no conflicts of interest.

Data availability

The data that support the findings of this study are available from the corresponding author upon reasonable request.

Supplementary information (SI) is available. See DOI: https://doi.org/10.1039/d5tc03478g.

Acknowledgements

This work was supported by the National Natural Science Foundation of China (grant no. 12204109) and the National Key Research and Development Program of China (grant no. 2021YFA1200700). Y. C. acknowledges the support from the Anhui Province University Research Project (grant no. 2023AH051194). Part of the experimental work has been carried out in the Fudan Nanofabrication Laboratory.

References

1 W. Pan, J. Zheng, L. Wang and Y. Luo, A future perspective on in-sensor computing, *Engineering*, 2022, **14**, 19–21.
2 Q. Ren, *et al.*, Optoelectronic devices for in-sensor computing, *Adv. Mater.*, 2025, **37**, 2407476.
3 Z. Ren, *et al.*, Near-sensor edge computing system enabled by a CMOS compatible photonic integrated circuit platform using bilayer AlN/Si waveguides, *Nano-Micro Lett.*, 2025, **17**, 261.
4 C. Choi, G. J. Lee, S. Chang, Y. M. Song and D.-H. Kim, Nanomaterial-based artificial vision systems: from bioinspired electronic eyes to in-sensor processing devices, *ACS Nano*, 2024, **18**, 1241–1256.
5 A. Sarker, T. Ul Islam and M. R. Islam, A review on recent trends of bioinspired soft robotics: actuators, control Methods, materials selection, sensors, challenges, and future prospects, *Adv. Intell. Syst.*, 2025, **7**, 2400414.
6 Y. Shi, N. T. Duong and K.-W. Ang, Emerging 2D materials hardware for in-sensor computing, *Nanoscale Horiz.*, 2025, **10**, 205–229.
7 M. Zhu, *et al.*, Promising functional two-dimensional lamellar metal thiophosphates: synthesis strategies, properties and applications, *Mater. Horiz.*, 2020, **7**, 3131–3160.
8 Z. Zhong, *et al.*, Reconfigurable logic circuits and rectifier based on two-terminal ionic homojunctions, *Device*, 2025, **3**, 100712.
9 Z. Zhong, *et al.*, Ionic-electronic photodetector for vision assistance with in-sensor image processing, *Nat. Commun.*, 2025, **16**, 7096.
10 Z. Zhong, *et al.*, Robust threshold-switching behavior assisted by Cu migration in a ferroionic $CuInP_2S_6$ heterostructure, *ACS Nano*, 2023, **17**, 12563–12572.
11 M. A. Susner, M. Chyasnavichyus, M. A. McGuire, P. Ganesh and P. Maksymovych, Metal thio- and selenophosphates as multifunctional van der Waals layered materials, *Adv. Mater.*, 2017, **29**, 1602852.
12 J. Chen, *et al.*, Mimicking neuroplasticity via ion migration in van der Waals layered copper indium thiophosphate, *Adv. Mater.*, 2022, **34**, 2104676.
13 X. Cheng, *et al.*, High precision conductance modulation in $CuCrP_2S_6$ synaptic devices for enhanced neuromorphic computing, *Adv. Funct. Mater.*, 2025, 2504017.
14 J. Wu, *Introduction to convolutional neural networks*, National Key Lab for Novel Software Technology, 2017, vol. 5, p. 495.
15 Z. Yu, *et al.*, van der Waals antiferroelectric $CuCrP_2S_6$-based artificial synapse for high-precision neuromorphic computation, *Small*, 2025, **21**, 2502676.
16 D. Cui, *et al.*, Coexistence of unipolar and bipolar resistive switching in optical synaptic memristors and neuromorphic computing, *Chip*, 2025, **4**, 100122.

17 D. Cui, *et al.*, Versatile optoelectronic memristor based on wide-bandgap Ga2O3 for artificial synapses and neuromorphic computing, *Light: Sci. Appl.*, 2025, **14**, 161.
18 X. Cheng, *et al.*, Ultra-low dark current photodetector based on two-dimensional $CuCrP_2S_6$ material, *Appl. Phys. Lett.*, 2025, **126**, 171105.
19 M. Susner, R. Rao, A. Pelton, M. McLeod and B. Maruyama, Temperature-dependent Raman scattering and x-ray diffraction study of phase transitions in layered multiferroic $CuCrP_2S_6$, *Phys. Rev. Mater.*, 2020, **4**, 104003.
20 W. F. Io, *et al.*, Direct observation of intrinsic room-temperature ferroelectricity in 2D layered $CuCrP_2S_6$, *Nat. Commun.*, 2023, **14**, 7304.
21 Y. Ma, *et al.*, High-performance van der Waals antiferroelectric $CuCrP_2S_6$-based memristors, *Nat. Commun.*, 2023, **14**, 7891.
22 Y. Guo, *et al.*, Electronic correlations in multiferroic van der Waals $CuCrP_2S_6$: Insights from X-ray spectroscopy and DFT, *J. Phys. Chem. C*, 2024, **128**, 7830–7839.
23 R. R. Ma, *et al.*, Nanoscale mapping of Cu-Ion transport in van der Waals layered $CuCrP_2S_6$, *ACS Appl. Mater. Interfaces*, 2022, **9**, 2101769.
24 X. Jing, *et al.*, Fabrication of scalable and ultra low power photodetectors with high light/dark current ratios using polycrystalline monolayer MoS_2 sheets, *Nano Energy*, 2016, **30**, 494–502.
25 L. Meng, *et al.*, Gate voltage dependence ultrahigh sensitivity WS_2 avalanche field-effect transistor, *IEEE Trans. Electron Devices*, 2022, **69**, 3225–3229.
26 Y. Ardeshirpour, M. J. Deen and S. Shirani, Evaluation of complementary metal-oxide semiconductor based photodetectors for low-level light detection, *J. Vac. Sci. Technol., A*, 2006, **24**, 860–865.
27 M. Hong, L. Dai, H. Hu and C. Li, Structural, ferroelectric, and electronic transitions in the van der Waals multiferroic material $CuCrP_2S_6$ under high temperature and high pressure, *Phys. Rev. B*, 2024, **110**, 144103.
28 Y. Huang, *et al.*, Cu^+ migration and resultant tunable rectification in $CuInP_2S_6$, *ACS Appl. Electron. Mater.*, 2023, **5**, 5625–5632.
29 X. Wang, *et al.*, Electrical and magnetic anisotropies in van der Waals multiferroic $CuCrP_2S_6$, *Nat. Commun.*, 2023, **14**, 840.
30 H. Qiao, *et al.*, Self-powered photodetectors based on 2D materials, *Adv. Opt. Mater.*, 2020, **8**, 1900765.
31 P. Zhang, *et al.*, Progress in 2D Material-Based Infrared Photodetectors for Intelligent Vision Applications, *Adv. Funct. Mater.*, 2025, 2502072.
32 G. Lee, *et al.*, Artificial neuron and synapse devices based on 2D materials, *Small*, 2021, **17**, 2100640.
33 C. Zhang, *et al.*, Recent progress on 2D materials-based artificial synapses, *Crit. Rev. Solid State Mater. Sci.*, 2022, **47**, 665–690.
34 X. Gao, *et al.*, Artificial Synapses and Logic Gates Based on Tellurium Oxide Memristors for Artificial Vision Applications, *Adv. Funct. Mater.*, 2025, e15165.
35 R. Yang, H. M. Huang and X. Guo, Memristive synapses and neurons for bioinspired computing, *Adv. Electron. Mater.*, 2019, **5**, 1900287.
36 Y. Sun, *et al.*, Internal ion transport in ionic 2D $CuInP_2S_6$ enabling multi-state neuromorphic computing with low operation current, *Mater. Today*, 2023, **66**, 9–16.
37 S. Zhao, *et al.*, Neuromorphic-computing-based adaptive learning using ion dynamics in flexible energy storage devices, *Nat. Sci. Rev.*, 2022, **9**, nwac158.
38 S. S. Kadam, A. C. Adamuthe and A. B. Patil, CNN model for image classification on MNIST and fashion-MNIST dataset, *J. Sci. Res.*, 2020, **64**, 374–384.
39 U. Saray and U. Çavdar, Comparison of different optimization algorithms in the fashion MNIST dataset, *Int. J. Multidiscip. Studies Innovative Technol.*, 2024, **8**, 52–58.
40 Y. Munakata and J. Pfaffly, Hebbian learning and development, *Dev. Sci.*, 2004, **7**, 141–148.
41 Y. Zhao, *et al.*, Anisotropy and synaptic plasticity in CrSBr/WSe_2 heterojunction for advanced neural network applications, *Rare Met.*, 2025, 1–11.
42 F. Yang, *et al.*, Reconfigurable High-Performance Memristors Based on Few-Layer High-κ Dielectric Bi_2SeO_5 for Neuromorphic Computing, *Adv. Funct. Mater.*, 2025, e14338.
43 J. Yang, *et al.*, Wafer-Scale Memristor Array Based on Aligned Grain Boundaries of 2D Molybdenum Ditelluride for Application to Artificial Synapses, *Adv. Funct. Mater.*, 2024, **34**, 2309455.
44 X. Liu, *et al.*, An optoelectronic synapse based on two-dimensional violet phosphorus heterostructure, *Adv. Sci.*, 2023, **10**, 2301851.
45 W. Li, *et al.*, Reconfigurable Multifunctional Semifloating Gate Transistors Based on the $ReSe_2$/h-BN/Graphene van der Waals Heterostructure, *ACS Appl. Mater. Interfaces*, 2025, **17**, 18623–18635.
46 F. Ordonez Morales, *et al.*, Modulating Synaptic Plasticity of Analogue Memristor Based on Oxidized MXene Composited with ZrO_2 Quantum Dots, *ACS Mater. Lett.*, 2025, **7**, 3997–4004.
47 R. Sun, *et al.*, Survey of image edge detection, *Front. Signal Process.*, 2022, **2**, 826967.
48 G. Feng, X. Zhang, B. Tian and C. Duan, Retinomorphic hardware for in-sensor computing, *InfoMat*, 2023, **5**, e12473.
49 F. Tu, *et al.*, Deep convolutional neural network architecture with reconfigurable computation patterns, *IEEE Trans. Very Large Scale Integr. Syst.*, 2017, **25**, 2220–2233.
50 Y. Nishitani, Y. Kaneko, M. Ueda, T. Morie and E. Fujii, Three-terminal ferroelectric synapse device with concurrent learning function for artificial neural networks, *J. Appl. Phys.*, 2012, **111**, 124108.
51 M. Si, *et al.*, A ferroelectric semiconductor field-effect transistor, *Nat. Electron.*, 2019, **2**, 580–586.
52 L. T. Pham, E. Oksum and T. D. Do, Edge enhancement of potential field data using the logistic function and the total horizontal gradient, *Acta Geod. Geophys.*, 2019, **54**, 143–155.
53 G. R. Cooper and D. R. Cowan, Edge enhancement of potential-field data using normalized statistics, *Geophysics*, 2008, **73**, H1–H4.
54 S. Anand, R. S. S. Kumari, T. Thivya and S. Jeeva, Sharpening enhancement of ultrasound images using contourlet transform, *Optik*, 2013, **124**, 4789–4792.